

Geometric valley Hall effect and valley filtering through a singular Berry fluxHong-Ya Xu,¹ Liang Huang,² Danhong Huang,^{3,4} and Ying-Cheng Lai^{1,5,*}¹*School of Electrical, Computer and Energy Engineering, Arizona State University, Tempe, Arizona 85287, USA*²*School of Physical Science and Technology, and Key Laboratory for Magnetism and Magnetic Materials of MOE, Lanzhou University, Lanzhou, Gansu 730000, China*³*Air Force Research Laboratory, Space Vehicles Directorate, Kirtland Air Force Base, New Mexico 87117, USA*⁴*Center for High Technology Materials, University of New Mexico, 1313 Goddard St SE, Albuquerque, New Mexico 87106, USA*⁵*Department of Physics, Arizona State University, Tempe, Arizona 85287, USA*

(Received 16 August 2016; revised manuscript received 12 June 2017; published 12 July 2017)

Conventionally, a basic requirement to generate valley Hall effect (VHE) is that the Berry curvature for conducting carriers in the momentum space be finite so as to generate anomalous deflections of the carriers originated from distinct valleys into different directions. We uncover a geometric valley Hall effect (gVHE) in which the valley-contrasting Berry curvature for carriers *vanishes completely* except for the singular points. The underlying physics is a singular non- π fractional Berry flux located at each conical intersection point in the momentum space, analogous to the classic Aharonov-Bohm effect of a confined magnetic flux in real space. We demonstrate that, associated with gVHE, exceptional skew scattering of valley-contrasting quasiparticles from a *valley-independent, scalar* type of impurities can generate charge-neutral, transverse valley currents. As a result, the massless nature of the quasiparticles and their high mobility are retained. We further demonstrate that, for the particular Berry flux of $\pi/2$, gVHE is considerably enhanced about the skew scattering resonance, which is electrically controllable. A remarkable phenomenon of significant practical interest is that, associated with gVHE, highly efficient valley filtering can arise. These phenomena are robust against thermal fluctuations and disorders, making them promising for valleytronics applications.

DOI: [10.1103/PhysRevB.96.045412](https://doi.org/10.1103/PhysRevB.96.045412)**I. INTRODUCTION**

In electronics and spintronics, information is encoded through charge and electronic spin, respectively. In addition to charge and spin, valley quantum numbers provide an alternative way to distinguish and designate quantum states, leading to the concept of valleytronics [1,2], an area that has attracted much recent interest [3–11]. Take graphene as an example, where the crystalline structure stipulates that uncharged degrees of freedom such as valley isospin can arise [12]. In the first Brillouin zone, there are two nonequivalent Dirac points \mathbf{K} and \mathbf{K}' , which are associated with distinct momenta or valley quantum numbers. The two nonequivalent valleys act as an ideal two-state system, which have a large momentum separation and are robust against external perturbations [2,13]. Electrons affiliated with the distinct valleys can be exploited for applications, e.g., in quantum information processing [14]. Appealing binary valley characteristics can also arise in other materials such as silicene and MoS_2 [6], graphene-inspired artificial crystals such as photonic graphene [15] that exhibits valley-polarized beams and sonic (phononic) crystals [9] in which valley vortex states can emerge, and valley photonic crystals [16].

In valleytronics, a fundamental issue is to separate the electrons with distinct valley quantum numbers, i.e., to create the so-called valley filters [1]. In graphene, due to its synthetic nature, the valley isospin can be manipulated for various valley filtering designs via strategies such as perfect zigzag edge confinements [1], staggered sublattice potentials [2], trigonal warping effect of the band structures [15], line defects [17],

and strain engineering [10,11,18–20]. A viable mechanism to realize valley filtering is through the valley Hall effect (VHE) [2,5,7,21–28], where electrons with different valley quantum numbers are separated and move in spatially distinct regions. Indeed, the Hall effect is one of the most fundamental phenomena in physics, and of particular relevance to VHE are the anomalous Hall effect (AHE) [29] and the spin Hall effect (SHE) [30–35]. There exist two types of mechanisms for AHE/SHE: intrinsic or extrinsic. The former in general has a topological origin, where finite momentum-space Berry curvatures (Berry flux densities) characterizing the topological invariants of the band structure of the material are linked, while the latter is typically caused by the skew (Mott) scattering or side-jump effect from the external impurities involving spin-dependent perturbations, e.g., spin-orbit coupling. SHE opens up an avenue for the conversion between electrical (charge) currents and spin (uncharged) currents, which played a key role in spintronics development for spin-current generators and detectors. Similar to SHE, associated with VHE, electrical currents can generate transverse valley currents and vice versa. In recent years, there have been theoretical [2,7,21–24] and experimental [5,25–28] studies of VHE. Due to the similarity between SHE and VHE, most existing theoretical proposals for VHE are based on essentially the same physical mechanism as for SHE [13,36], where either bulk or local *valley-resolved perturbations* are required.

For the honeycomb lattice system, the semiclassical picture based on finite valley-contrasting Berry curvatures stipulates that valley-resolved gap opening perturbations are necessary for VHE and valley filtering [2,23]. Alternative mechanisms for VHE require external magnetic fields, strain-induced pseudomagnetic fields, or magnetic materials that have an opposite effect on the two valleys [10,11,18–20]. We ask

*Ying-Cheng.Lai@asu.edu

the following question: When Berry curvatures vanish, does nontrivial valley-contrasting physics exist without *any* valley-resolved perturbation? The purpose of this paper is to provide an affirmative answer. Our success in uncovering a valley-free perturbation mechanism for VHE, and valley filtering relies on two basic observations: (i) the classic Aharonov-Bohm effect can be induced by a singular line of magnetic flux with vanishing magnetic field away from it, and (ii) the Berry curvature (Berry flux density) can be regarded as the geometric analog of the magnetic field (magnetic flux density) in the momentum space [37,38]. Specifically, analogous to a confined magnetic flux generated by an infinitely narrow solenoid, the Berry flux arising from a conical intersection (singularity) in the energy-momentum spectrum is perfectly localized at the diabolical point with a specific valley quantum number. The Berry phase acquired along a loop enclosing the point can then be defined but, away from the point, the Berry curvature vanishes everywhere. Due to time-reversal symmetry, the singular Berry fluxes associated with the nonequivalent valleys carry opposite signs. As a result, if two valleys possess a singular non- π fractional Berry flux with opposite signs, different Berry phases can be acquired along the closed loop induced by, e.g., a scattering process, leading to valley-resolved interference patterns. We stress that such valley-contrasting effects are originated from the singular nature of the underlying band structure in the absence of any finite Berry curvature away from the singular points without imposing any constraint on the type of the scattering that can be completely valley independent.

Here, we present a VHE with which an efficient valley filtering effect can arise via spatially valley-contrasting interference. Due to the geometric nature of the underlying mechanism, we name the phenomenon gVHE where, when the momentum-space singular Berry flux is non- π fractional, charge-neutral valley currents are generated from exceptional skew scattering from a *valley-independent, scalar type of impurities*. The gVHE is neither purely intrinsic nor purely extrinsic, but of a mixed type. As such, our result is beyond existing knowledge and represents a fundamentally different phenomenon. To be concrete, we focus on α - \mathcal{T}_3 lattices that host massless Dirac-type particles with a variable singular Berry flux and show that there is a nonlinear dependence of the valley Hall angle on the Berry flux with asymmetrically resonant features. For the particular singular Berry flux of $\pi/2$, gVHE is considerably enhanced, which occurs near a resonance associated with skew scattering and can be electrically controlled by varying the Fermi energy or the scatterer strength. We develop a physical understanding of the resonant skew scattering, which is nonperturbative and much stronger than the conventional skew scattering predicted by a third- or higher-order perturbation theory. We further show that gVHE is robust against thermal fluctuations and disorders, making it promising for valleytronic applications.

II. HAMILTONIAN AND METHODS

Effective Hamiltonian. We consider a generalized lattice system (i.e., α - \mathcal{T}_3) interpolating between a graphene and a dice lattice. The effective low-energy Hamiltonian is

given by [39]

$$H_0 = \hbar v_F (\tau_3 \otimes S_x^\alpha k_x + \tau_0 \otimes S_y^\alpha k_y), \quad (1)$$

where v_F is the Fermi velocity, $\mathbf{k} = (k_x, k_y)$ denotes the two-dimensional (2D) wave vector measured about one of the two nonequivalent valleys (\mathbf{K} or \mathbf{K}') at a corner of the hexagonal Brillouin zone, and the Pauli matrices $\tau_{1,2,3}, \tau_0 = I_{2 \times 2}$ act on the valley degree of freedom representing an emergent isospin. The matrices S_x^α and S_y^α (explicit forms in Appendix A) parametrized by $\alpha = \tan \phi$ identify the nonequivalent crystalline sublattices. The Hamiltonian H_0 acts on the six-component spinor $\Psi = [\Psi_A^\tau, \Psi_B^\tau, \Psi_C^\tau, \Psi_A^{\tau'}, \Psi_B^{\tau'}, \Psi_C^{\tau'}]^T$. The energy spectrum consists of three bands: a dispersionless flat band $E_0(\mathbf{k}) = 0$ and two linearly dispersive bands $E_s(\mathbf{k}) = s \hbar v_F |\mathbf{k}|$ with $s = \pm 1$ being the band index, where the latter are identical to the low-energy bands of graphene that give rise to massless excitations.

Due to the $\alpha \rightarrow 1/\alpha$ (or $\phi \rightarrow \pi/2 - \phi$) duality of the model, we restrict our study to the regime $\alpha \in [0, 1]$. Note that the resulting zero-field spectrum is α independent and features isotropic linear band crossings, while H_0 describes different low-energy excitations characterized by an α -dependent Berry phase upon winding of the band-touching point \mathbf{K} or \mathbf{K}' . In the momentum space, the Berry phase underlying the n th energy band belonging to one of the valleys with a valley index $\tau = \pm 1$ is defined as $\Phi_n^\tau = \oint d\mathbf{k} \cdot \mathcal{A}_n^\tau$ with $\mathcal{A}_n^\tau = \langle \Psi_{n,\mathbf{k}}^\tau | i \nabla_{\mathbf{k}} | \Psi_{n,\mathbf{k}}^\tau \rangle$ being the Berry connection (acting as a vector potential in momentum space). Quantitatively, we obtain $\Phi_s^\tau = \tau(1 - \alpha^2)/(1 + \alpha^2)\pi$ for the conical bands and $\Phi_0^\tau = -2\tau(1 - \alpha^2)/(1 + \alpha^2)\pi$ for the flat band (see Appendix B). Two particular cases arise for $\alpha = 0$ ($\phi = 0$) and $\alpha = 1$ ($\phi = \pi/4$). In the former, the system corresponds to a graphene system with an extra inert flat band effectively governed by a reduced Hamiltonian in the block-diagonal form $H_0 = \hbar v_F (\tau_3 \otimes \sigma_x k_x + \tau_0 \otimes \sigma_y k_y) \oplus 0$, with the Pauli matrices $\sigma_{x,y}$ accounting for the effective sublattice degrees of freedom. In the latter case, the system is a dice lattice hosting massless pseudospin-1 quasiparticles with a vanishing Berry phase, where the matrices $S_{x,y}^{\alpha=1}$ satisfy the spin-1 algebra. From the point of view of symmetry, the two cases belong, respectively, to the classes $SU(2) \otimes [SU(2) \oplus SU(1)]$ and $SU(2) \otimes SO(3)$. In the intermediate regime $0 < \alpha < 1$, the matrices $S_{x,y}^\alpha$ in H_0 do not obey the algebra of angular momentum, nor any other closed algebra. As such, with more than a single pseudospin operator in general, H_0 cannot be reduced to any known case of relativistic particles (spin-1 or spin- $\frac{1}{2}$) but is an admixture (hybrid) of them with a non- π fractional Berry phase. Remarkably, the Berry phases associated with the two nonequivalent valleys are different except for the particular cases of $\alpha = 0, 1$. In addition, we note that the Berry curvature $\Omega_{\mathbf{k}}^\tau = \nabla_{\mathbf{k}} \times \mathcal{A}_{\mathbf{k}}^\tau$ (acting as a ‘‘magnetic’’ field in the momentum space) is always zero away from the gapless point \mathbf{K} or \mathbf{K}' . Specifically, as derived in Appendix B, it takes on a singular form as

$$\Omega_{s,\mathbf{k}}^\tau = \tau \frac{1 - \alpha^2}{1 + \alpha^2} \pi \delta(\mathbf{k}) \hat{k}_z \equiv \tau \Phi \pi \delta(\mathbf{k}) \hat{k}_z, \quad (2)$$

where s is the index of the conical bands, τ is the valley index of \mathbf{K} ($\tau = 1$) and \mathbf{K}' ($\tau = -1$). The quantity Φ denotes the flux magnitude in units of π , and a singular non- π fractional Berry

flux means $0 < \Phi < 1$, where a valley-contrasting Berry phase of $\tau\Phi\pi$ can be acquired along any circuit enclosing a single Dirac point belonging to one of the valleys. Analogously, the resulting Berry curvature given in Eq. (2) acts as a tunable ‘‘Aharonov-Bohm flux line’’ of magnitude Φ applied perpendicular to the 2D momentum space, which will not exert the local ‘‘deflecting force’’ away from it but will result in a nontrivial Berry phase depending on the circuit about the ‘‘flux line’’. In this regard, the typical Dirac cones emerging from the hexagonal lattice are effectively a singular π Berry flux localized at the Dirac point [38], while those in the $\alpha\text{-}\mathcal{T}_3$ lattice can give rise to a singular non- π fractional Berry flux in general. Since the underlying Berry curvature vanishes except at the Dirac points that form a set of measure zero in the 2D momentum space, we can rule out an anomalous Hall effect of the intrinsic type as argued in existing works [2,29,35].

Semiclassical transport. To investigate the charge and valley transport properties, we analyze the semiclassical Boltzmann transport equation (BTE) which, in the presence of an applied uniform electric field $\mathcal{E} = \mathcal{E}\mathbf{e}_x$, takes the form [40]

$$-e\mathcal{E} \cdot \mathbf{v}_{\mathbf{k}} \frac{\partial n^0}{\partial E} = \sum_{\mathbf{k}', \tau'} [n_{\tau}(\mathbf{k}) - n_{\tau'}(\mathbf{k}')] W_{\tau'\tau}(\mathbf{k}', \mathbf{k}), \quad (3)$$

where $-e < 0$ is the electron charge, $\mathbf{v}_{\mathbf{k}} = (1/\hbar)\nabla_{\mathbf{k}}E_{\mathbf{k}}$ is the band velocity, $n^0 = 1/[\exp(E - \mu)/k_B T + 1]$ denotes the equilibrium Fermi-Dirac distribution, and $n_{\tau}(\mathbf{k})$ is the distribution function for carriers with momentum \mathbf{k} and valley index τ . Impurities distributed at random positions of scattering centers \mathbf{r}_i with a dilute concentration (areal density) n_{imp} are described by the disordered potential $V(\mathbf{r}) = \sum_i V^{(i)}(\mathbf{r} - \mathbf{r}_i)$, and the quantum scattering rate off the potential from the state $|\mathbf{k}, \tau\rangle$ to the state $|\mathbf{k}', \tau'\rangle$ is $W_{\tau'\tau}(\mathbf{k}', \mathbf{k}) = (4\pi^2 \hbar v_g^2 n_{\text{imp}} / k) |f_{\tau\tau'}(\theta)|^2 \delta(E_{\mathbf{k}} - E_{\mathbf{k}'})$, where $f_{\tau\tau'}(\theta)$ is the scattering amplitude at the angle $\theta = \arccos(\mathbf{k} \cdot \mathbf{k}' / k^2)$. Skew scattering means an asymmetry in the scattering amplitude $f_{\tau\tau'}(\theta) \neq f_{\tau\tau'}(-\theta)$, which leads to $W_{\tau\tau'}(\mathbf{k}', \mathbf{k}) \neq W_{\tau'\tau}(\mathbf{k}, \mathbf{k}')$. Defining $\delta n_{\tau}(\mathbf{k}) = n_{\tau}(\mathbf{k}) - n^0$ as the deviation of the valley-dependent distribution function from its equilibrium value, in the linear response regime we impose the following ansatz for isotropic Fermi surfaces in the conduction (valence) band $s = 1$ ($s = -1$): $\delta n_{\tau}(\mathbf{k}) = s v_F [A_{\tau} \cos \varphi(\mathbf{k}) + B_{\tau} \sin \varphi(\mathbf{k})]$, where $\varphi(\mathbf{k})$ is the angle that the momentum vector \mathbf{k} makes with the direction of the external electric field \mathcal{E} , A_{τ} and B_{τ} are coefficients. Substituting this ansatz into Eq. (3) and setting $\varphi(\mathbf{k}) = 0$ [$\varphi(\mathbf{k}) = \pi/2$] for the longitudinal (transverse) response, we obtain a closed-form solution of the linearized BTE. The current due to the external driving electric field can be calculated explicitly as $\mathbf{j}_{\tau} = -egS/(2\pi)^2 \int d^2\mathbf{k}' \delta n_{\tau}(\mathbf{k}) \mathbf{v}_{\mathbf{k}}$ with $g = 2$ and S being the spin degeneracy and the given sample area, respectively. The steady-state charge (longitudinal) and valley Hall (transverse) currents are then given by $j_x = \sum_{\tau} \mathbf{j}_{\tau} \cdot \mathbf{e}_x \equiv \sigma^{xx} |\mathcal{E}|$ and $j_{vH} = \sum_{\tau} \tau \mathbf{j}_{\tau} \cdot \mathbf{e}_y \equiv \sigma_{vH}^{yx} |\mathcal{E}|$, where the valley Hall and the longitudinal conductivities are given by

$$\sigma_{vH}^{yx} = -e^2 \frac{g}{2\hbar} \sum_{\tau=\pm} \int dE |E| \frac{\partial n^0}{\partial E} \frac{\tau \xi_{sk}^{\tau}}{1 + (\xi_{sk}^{\tau} / \xi_{tr}^{\tau})^2} \quad (4)$$

and

$$\sigma^{xx} = -e^2 \frac{g}{2\hbar} \sum_{\tau=\pm} \int dE |E| \frac{\partial n^0}{\partial E} \frac{\xi_{tr}^{\tau}}{1 + (\xi_{tr}^{\tau} / \xi_{sk}^{\tau})^2}, \quad (5)$$

respectively, with the usual transport (longitudinal) relaxation time ξ_{tr}^{τ} and the skew (transverse) relaxation time ξ_{sk}^{τ} determined by $1/\xi_{tr}^{\tau} = (2\pi)^{-2} \int d^2\mathbf{k}' (1 - \cos \theta) W_{\tau\tau}(\mathbf{k}', \mathbf{k})$ and $1/\xi_{sk}^{\tau} = (2\pi)^{-2} \int d^2\mathbf{k}' \sin \theta W_{\tau\tau}(\mathbf{k}', \mathbf{k})$, respectively. The valley Hall angle characterizing the efficiency of the charge current to valley current conversion is given by

$$\gamma \equiv \frac{j_{vH}}{j_x} = \frac{\sigma_{vH}^{yx}}{\sigma^{xx}}, \quad (6)$$

which at zero temperature reduces to the ratio $\xi_{tr}^{\tau} / \xi_{sk}^{\tau}$ and can be expressed in terms of the pertinent scattering cross sections with respect to a single scattering event: $\gamma|_{T=0} = \Sigma_{sk}^{\tau} / \Sigma_{tr}^{\tau}$, where the skew and transport cross sections are given, respectively, by $\Sigma_{sk}^{\tau} = \int d\theta \sin \theta |f_{\tau\tau}(\theta)|^2$ and $\Sigma_{tr}^{\tau} = \int d\theta |f_{\tau\tau}(\theta)|^2 (1 - \cos \theta)$.

III. RESULTS

We model the impurities as an ensemble of dilute disk scatterers of radius R described by the scalar potential

$$V^{(i)}(\mathbf{r}) = \tau_0 \otimes \mathcal{I} V_0 \Theta(R - |\mathbf{r} - \mathbf{r}_i|) \quad (7)$$

located at random positions \mathbf{r}_i , where V_0 is the potential height and \mathcal{I} is an identity matrix acting on the sublattice space. Note that the impurities are neither valley nor sublattice dependent and they do not affect the massless nature of the carriers associated with the conical bands. As a result, high mobility of the carriers is retained. Scattering properties from a single impurity can be treated without the need to use perturbation theory, as presented in Appendix C. A quantitative understanding of underlying transport can be obtained through the Boltzmann transport formalism described in Sec. II. Based on quantitative analyses and calculations, we demonstrate in a concrete manner the main findings stated in the last paragraph of Sec. I.

A. Exceptional valley skew-scattering-induced geometric valley Hall effect

We first show that a surprising valley skew scattering effect can arise for the case of singular non- π fractional Berry flux. Quantitatively, such a valley-resolved asymmetric scattering process from the state $|\mathbf{k}, \tau\rangle$ to the state $|\mathbf{k}', \tau'\rangle$ can be characterized by the skew cross section $\Sigma_{sk}^{\tau} = \int d\theta \sin \theta |f_{\tau\tau}(\theta)|^2$ with $f_{\tau\tau}(\theta)$ being the scattering amplitude at the angle $\theta = \arccos(\mathbf{k} \cdot \mathbf{k}' / k^2)$. The skew cross section turns out to be finite for the flux magnitude in the range $0 < \Phi < 1$ and attains significant values about the resonant scattering point [cf. Eq. (D5) in Appendix D]. This is striking because the scattering asymmetry in the valley-coded binary channels emerges from an isotropic, valley-free electrostatic scatterer *in the absence of any valley-dependent perturbation*. Moreover, the physical effect is not of any perturbative type, which is remarkable considering that a previous third-order perturbation theory predicted [29] only small values for the skew scattering cross section. In our case, the resulting sizable

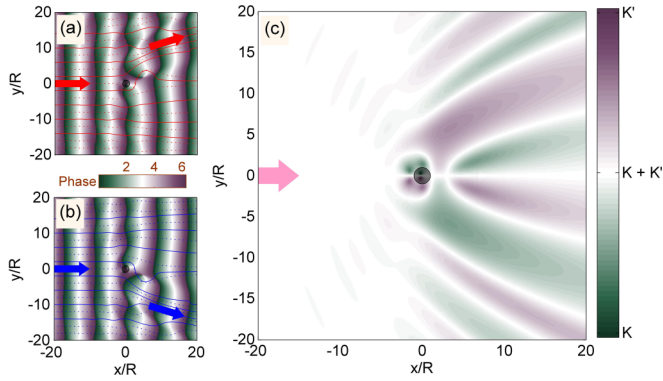


FIG. 1. Exceptional valley skew scattering from a valley-independent scalar-type scatterer. The two valleys are \mathbf{K}' and \mathbf{K} in (a) and (b), respectively, which are distinguished in terms of the spatially resolved phases of the second component of the corresponding wave functions. The red (blue) arrow and streamlines denote the propagation direction of quasiparticles from the valley \mathbf{K}' (\mathbf{K}). The scalar scatterer is represented as the gray shaded disk. (c) Spatially valley-resolved intensity distribution of the resulting interference/diffraction pattern. Panels (a)–(c) are for a singular Berry flux of $\pm\pi/2$ with the following scattering parameters: relative incident energy $E/V_0 = 0.7268$ and effective scatterer strength $V_0R = 1$.

valley skew scattering behavior has a different physical origin that is associated with the valley-dependent Berry phase caused by the singular Berry flux in terms of any trajectory enclosing a single conical intersection point with one of the valleys centered. As a result, for a given scattering process with specific momenta, carriers from the two nonequivalent valleys can acquire different nontrivial phases, with which a spatially valley-resolved wave scattering pattern emerges. A representative physical picture of the exceptional valley skew scattering process is demonstrated in Fig. 1 for a singular non- π fractional Berry flux case (i.e., $\Phi = \frac{1}{2}$).

Associated with the *exceptional* valley skew scattering, a VHE can arise. In particular, as the hallmark of any skew scattering, a finite value of Σ_{sk}^r means a kind of asymmetry characterized by $|f_{\tau\tau}(\theta)| \neq |f_{\tau\tau}(-\theta)|$ for carriers belonging to a given valley τ ($\tau = \pm$). In addition, the preservation of the time-reversal symmetry imposes a mirror symmetry $|f_{\tau\tau}(\theta)| = |f_{\bar{\tau}\bar{\tau}}(-\theta)|$ on different valleys. Both factors contribute to the spatial separation of the valley degree of freedom of carriers and lead to the emergence of a transverse valley current with zero net charge. The VHE can be quantified by the valley Hall angle (VHA) γ , the ratio of the valley Hall conductivity to the longitudinal conductivity [cf. Eqs. (4) and (5) in Sec. III]. Effectively, γ is a figure of merit characterizing the efficiency of net transverse valley current conversion. A better understanding of the skew scattering mechanism can be obtained from the closed form of VHA at zero temperature given by

$$\gamma|_{T=0} = \Sigma_{sk}^r / \Sigma_{lr}^r.$$

It follows from the expression that a finite VHA and hence VHE arise from effective valley skew scattering from a scalar type of impurities in the absence of any valley-dependent per-

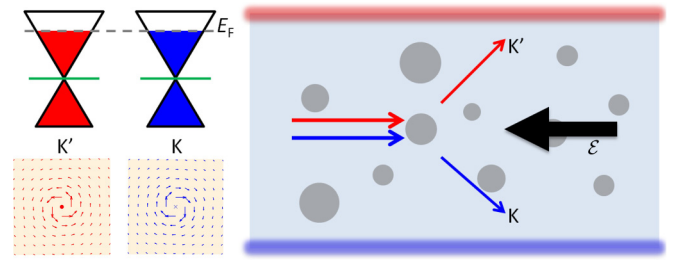


FIG. 2. A schematic illustration of geometric valley Hall effect (gVHE) induced by skew scattering from impurities (gray shaded disks). This type of Hall effect is *mixed* that is mediated by the inherent singular Berry flux and manifests itself with exceptional valley skew scattering from valley-independent scalar-type impurities.

turbations, as shown schematically in Fig. 2, where a singular non- π fractional Berry flux is located at each center of the two nonequivalent valleys in the momentum space. We note that the origin of the proposed VHE can be attributed to the singular Berry flux leading to valley-resolved quasiparticle scattering with distinct Berry phase accumulations but vanishing Berry curvature. This is analogous to the Aharonov-Bohm effect induced by a confined real magnetic flux without any magnetic field exerted outside (hence the name gVHE).

B. Dependence of VHA on singular Berry flux

Quantitatively, the emergence of gVHE can be ascertained through the dependence of the characteristic VHA γ on the singular Berry flux magnitude Φ . We calculate VHA at zero temperature and show its contour map versus the relative carrier energy E/V_0 and Φ in Fig. 3(a). There are finite VHAs

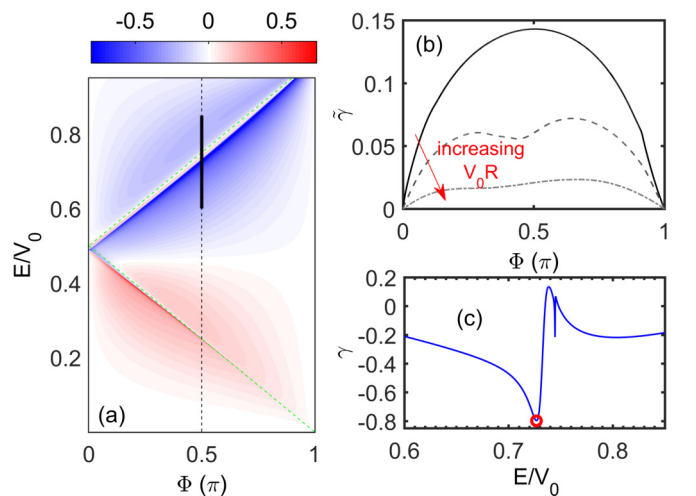


FIG. 3. Singular Berry flux defined valley Hall angle. (a) Contour map of valley Hall angle γ versus the singular Berry flux magnitude Φ and the relative energy E/V_0 for scatterer strength $V_0R = 1$. (b) Average valley Hall angle $\tilde{\gamma}$ over the Fermi energy versus the Berry phase for different values of the scatterer strength as represented by the solid line ($V_0R = 1$), the dashed line ($V_0R = 10$), and the dotted-dashed line ($V_0R = 100$). (c) Enhancement of VHA due to resonant valley skew scattering occurring within the energy range indicated by the thick black line in (a) for $\Phi = \frac{1}{2}$ and $V_0R = 1$.

($\gamma \neq 0$) within the range $0 < \Phi < 1$, which correspond to a non- π fractional Berry flux leading to a non- π fractional Berry phase but a zero Berry curvature away from the Dirac point, say for $E/V_0 > 0$. In addition, in the two limiting cases with singular Berry fluxes of 0 and π (i.e., $\Phi \rightarrow 0, 1$), we have $\gamma \rightarrow 0$. Note that the former and latter cases correspond, respectively, to a dice lattice system with massless pseudospin-1 low-energy excitations and a graphene system hosting massless pseudospin- $\frac{1}{2}$ quasiparticles. By definition, $\gamma = 0$ means that the Hall effect vanishes, and a large value of $|\gamma|$ indicates a strong VHE. In addition, at zero temperature, $\gamma|_{T=0}$ is effectively the transport skewness that characterizes the degree of asymmetry in the associated scattering event. As such, we have that the gVHE emerges due to the singular non- π fractional Berry flux that permits exceptional valley skew scattering from valley-independent, scalar type of scatterers. At low energies, i.e., $kR \ll 1$, for $E/V_0 \ll 1$, we obtain an analytic formula for the VHA versus the flux magnitude (see Appendix D for the derivations and its validation):

$$\gamma(\Phi) \simeq \frac{\pi x^2 \frac{\Phi(1-\Phi)}{1+\Phi}}{(1+\eta)^2 [\Phi - (1-2\eta)]^2 + 4\eta \frac{\Phi(1-\Phi)}{1+\Phi}}, \quad (8)$$

where $\eta = E/V_0$ and $x = kR$. We see that the VHA exhibits a nonlinear dependence on the Berry flux and an asymmetric resonance profile. In particular, as Φ is increased from 0 to 1 monotonously, the VHA reaches maximum at $\Phi_* \simeq (1-2\eta)$, followed by a decrease to zero. Asymptotic behaviors at the opposite limits of $\Phi \rightarrow 1$ and $\Phi \rightarrow 0$ derived from Eq. (8) are $\gamma(\Phi) \sim (1-\Phi)$ for $\Phi \rightarrow 1$ and $\gamma \sim \Phi$ for $\Phi \rightarrow 0$. We see that the VHA vanishes linearly as $\Phi \rightarrow 0, 1$, i.e., when the π -quantized Berry flux is recovered. Away from these limiting cases, gVHE emerges following an asymmetrically resonant behavior that has a nonlinear dependence on the singular Berry flux. Relaxing the assumption of $E/V_0 \ll 1$, we obtain an estimation of the other resonance position for $E/V_0 > \frac{1}{2}$ as $\Phi_* \simeq (2\eta - 1)$ (see Appendix D). Both theoretical predications are marked by the green dashed line in Fig. 3(a), where, on the other hand, the linear dependence of the resonance position on the Berry flux can be utilized to demarcate the unusual Berry phase associated with the quasiparticles through Hall transport measurements.

Figure 3(b) reveals the effect of the scatterer strength V_0R on gVHE, where the averaged absolute VHA $\bar{\gamma} \equiv \int |\gamma| dE / \int dE$ versus Φ for three different values of V_0R (1, 10, 100) is shown, as indicated by the solid, dashed, and dotted-dashed lines, respectively. We see that, on average, weak scatterers favor sizable VHAs, giving rise to a pronounced gVHE, while strong scatterers do not. An intuitive picture behind this can be obtained by resorting to the general summation form of the skew cross section in terms of the scattering phase shift δ_l : $\Sigma_{sk}^\tau = 4/k \sum \sin \delta_l \sin \delta_{l+\tau} \sin(\delta_l - \delta_{l+\tau})$ where, for a given carrier energy value E/V_0 , the larger V_0R is, the more scattering channels with different phase shifts are excited. As a result, there are many sign changes in δ_l or $(\delta_l - \delta_{l+\tau})$, reducing significantly the summation and hence VHA. This phenomenon is essentially due to the phase effect and is dominant in the long-wavelength limit. In particular, from Fig. 3(c), we see that the VHA can be enhanced significantly due to the emergent resonant valley skew scattering in the

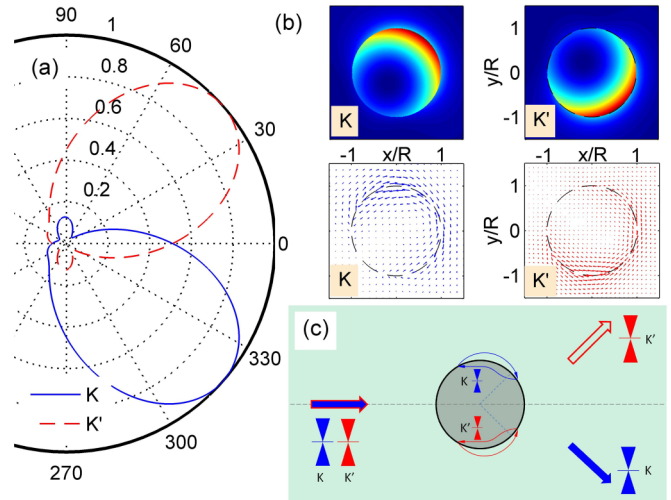


FIG. 4. Illustration of resonant skew-scattering-assisted valley filtering. For $\Phi = \frac{1}{2}$ with the resonance position indicated by the small red circle in Fig. 3(c), (a) polar plot of normalized differential cross section as a function of the scattering angle for different valleys: **K** (solid blue line) and **K'** (red dashed line), (b) associated near-field patterns of the local probability density belonging to different valleys (top two panels) and the corresponding current density plots (bottom ones), and (c) a schematic illustration of gVHE associated with resonant valley skew scattering.

energy domain, which can be achieved by controlling the Fermi energy.

C. Enhanced valley filtering through resonant skew scattering

Accompanying the enhancement in the VHA at skew scattering resonances, a sizable valley filtering effect will be anticipated. Insights into resonant skew-scattering-assisted valley filtering can be gained by investigating both the far-field and near-field behaviors in terms of the differential cross section (DCS) $d\Sigma^\tau/d\theta = |f_{\tau\tau}(\theta)|^2$ and the associated near-field patterns for different valleys, as illustrated in Figs. 4(a) and 4(b), respectively. There is an exact mirror symmetry with respect to the horizontal axis between the patterns associated with different valleys: an exact manifestation of the time-reversal symmetry. From the formula for $\gamma|_{T=0}$, we note that a large VHA implies a left-right asymmetry in the DCS and hence gives rise to a strong valley polarization along the azimuthal direction, and vice versa. Demonstration using a polar plot of DCS is displayed in Fig. 4(a) with resonance parameters indicated by the red circle in Fig. 3(c). As a result, a remarkable valley filtering/polarization effect emerges together with VHA enhancement and gVHE. Furthermore, it can be seen from Fig. 4(b) that, at the given resonance, valley-contrasting spatial skew (asymmetric) trappings occur via the formation of unusual fusiform vortices on one side of the boundary. Consequently, the scatterer only blocks one of the valleys effectively at one side via valley-dependent skew trapping, making the system an effective valley filter near the resonance. Figure 4(c) illustrates schematically the valley filtering mechanism due to resonant skew-scattering-enhanced gVHE. We also find that exceptionally large VHAs and strong

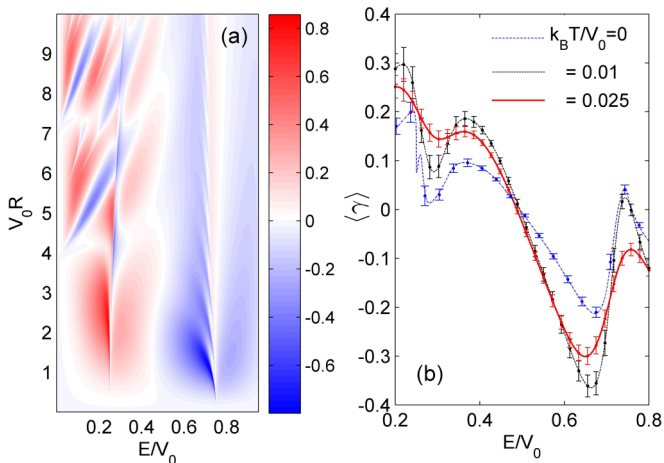


FIG. 5. Exceptionally large VHAs and the effect of thermal fluctuations and disorder averaging. For $\Phi = \frac{1}{2}$, (a) a contour plot of the VHA γ versus E/V_0 and the scatterer strength V_0R at zero temperature, and (b) ensemble-averaged VHA over scatterers with randomly distributed strength $V_0R \in (0, 10]$ versus the reduced Fermi energy for different values of the normalized thermal temperature $k_B T/V_0 = 0, 0.01, 0.025$.

valley filtering can occur for intermediate scatterer strength [cf. Fig. 7(a) in Appendix D].

D. Robustness against disorder averaging and thermal fluctuations

A further analysis of the effect of scatterer strength reveals that gVHE enhancement induced by resonant skew scattering is significant for intermediate scatterer strength, say $V_0R \sim 2$, where large VHAs with the maximum absolute value $|\gamma|_{\max} \sim 0.8$ can arise, as shown in Fig. 5(a). The Hall angle values are much larger than those for metals [41–45] ($|\gamma| \sim 0.01$ – 0.1) and for graphene [46–48] ($|\gamma| \sim 0.2$). This remarkable result holds in the presence of thermal fluctuations and disorder averaging, as shown in Fig. 5(b), rendering the phenomenon uncovered here promising for valleytronics applications.

IV. DISCUSSION

We uncover a singular momentum-space Berry flux mediated mechanism for VHE and show that it can lead to efficient, electrically controllable valley filtering without compromising the high mobility of the carriers, which is far more advantageous than the conventional approach of introducing a finite quasiparticle mass or deforming the underlying energy dispersion. In particular, for fractional Berry fluxes charge neutral transverse valley currents can be generated from exceptional skew scattering from a valley-independent, scalar type of impurities. Analogous to the Aharonov-Bohm effect mediated by a singular magnetic flux in the physical space, the VHE has a geometric origin associated with the underlying momentum-space Berry phase but vanishing Berry curvature. We develop an analytic understanding of the phenomena of gVHE and valley filtering, for which further physical insights can be gained by resorting to symmetry considerations (Appendix E). We demonstrate that gVHE and the resulting

valley filtering are robust against thermal fluctuations and disorders while preserving the high mobility of the carriers, potentially opening a door to developing faster and more efficient valleytronics.

It is worth emphasizing that the phenomenon of gVHE uncovered in this work belongs to the mixed type and emerges in the absence of any valley-resolved perturbation. To our best knowledge, this differs from any of the previous cases (Appendix F). We also remark that intervalley scattering can be neglected in our analysis, for the following two reasons: (1) a relatively large momentum transfer on the order of the inverse lattice spacing is needed to scatter a carrier from the K valley to the K' valley and (2) it is physically reasonable to assume that the impurity potentials are smooth on the lattice scale but sharp in comparison with the carriers' wavelength (Appendix G).

While we have used the α - \mathcal{T}_3 lattice to demonstrate our findings, we expect them to arise generally in physical systems hosting massless Dirac-type particles with a singular non- π fractional Berry flux in the momentum space. For instance, there exists a correspondence between our model and *massless Kane fermion* systems [49,50] that can arise in three-dimensional (3D) zinc-blende crystals, i.e., $\text{Hg}_{1-x}\text{Cd}_x\text{Te}$, at some critical doping concentration [51–53]. In particular, for singular Berry flux $\Phi = \frac{1}{2}$ ($\alpha = 1/\sqrt{3}$), we have $H_0(\alpha = 1/\sqrt{3}) \equiv \mathcal{H}_{\text{Kane}}(\mathbf{k}, k_z = 0)$ (see Appendix H). In this sense, the phenomenon of gVHE uncovered here manifests itself as the *geometric* SHE in a massless Kane fermion system, which can be experimentally validated in the 3D zinc-blende crystals in the presence of spin-independent (scalar-type) cylindrical symmetric impurities (e.g., charged dislocation line defects along the [001] direction).

ACKNOWLEDGMENTS

We acknowledge financial support from the Vannevar Bush Faculty Fellowship program sponsored by the Basic Research Office of the Assistant Secretary of Defense for Research and Engineering and funded by the Office of Naval Research through Grant No. N00014-16-1-2828. L.H. was supported by NSF of China under Grant No. 11422541.

APPENDIX A: EXPLICIT FORM OF MATRICES S_x^α AND S_y^α

The matrices S_x^α and S_y^α are given by

$$S_x^\alpha = \begin{pmatrix} 0 & \cos \phi & 0 \\ \cos \phi & 0 & \sin \phi \\ 0 & \sin \phi & 0 \end{pmatrix} \quad (\text{A1})$$

and

$$S_y^\alpha = \begin{pmatrix} 0 & -i \cos \phi & 0 \\ i \cos \phi & 0 & -i \sin \phi \\ 0 & i \sin \phi & 0 \end{pmatrix}, \quad (\text{A2})$$

which are parametrized by $\alpha = \tan \phi$. They identify the nonequivalent crystalline sublattices in the α - \mathcal{T}_3 lattice.

APPENDIX B: BERRY PHASE AND CURVATURE

We follow the recent works [39,49,50] to carry out calculations to show that, in our α - \mathcal{T}_3 system, the Berry curvature and phase are not conventional in the sense that the phase can be a fraction of π . The effective Hamiltonian in the main text is

$$H_0(\mathbf{k}) = \tilde{\alpha} \cdot \mathbf{k}, \quad (\text{B1})$$

where $\mathbf{k} = (k_x, k_y, 0)$ and $\tilde{\alpha} = (\tau_3 \otimes S_x^\alpha, \tau_0 \otimes S_y^\alpha, \tau_1 \otimes \tilde{S}_z)$ with $\tilde{S}_z = 0 \oplus \sigma_x$. The Hamiltonian H_0 has eigenvalues $E = n|\mathbf{k}|$ with $n = 0, \pm$ denoting the band index, and the associated eigenstates are given by

$$|\mathbf{k}, s\rangle|\tau\rangle = \frac{1}{\sqrt{2}} \begin{pmatrix} \tau \cos \phi e^{-i\tau\theta} \\ s \\ \tau \sin \phi e^{i\tau\theta} \end{pmatrix} |\tau\rangle \quad (\text{B2a})$$

for $E = s|\mathbf{k}|$ with $s = \pm$, and

$$|\mathbf{k}, 0\rangle|\tau\rangle = \begin{pmatrix} \tau \sin \phi e^{-i\tau\theta} \\ 0 \\ -\tau \cos \phi e^{i\tau\theta} \end{pmatrix} |\tau\rangle \quad (\text{B2b})$$

for $E = 0$, where $\tan \theta \equiv k_y/k_x$ and $\tau = \pm$ denotes the valley index. The Berry connection (field) of each band can be calculated from the definition $\mathcal{A}_{n,\mathbf{k}}^\tau = \langle \tau | \langle \mathbf{k}, n | \nabla_{\mathbf{k}} | \mathbf{k}, n \rangle | \tau \rangle$. We have

$$\mathcal{A}_{0,\mathbf{k}}^\tau = -\tau \frac{1 - \alpha^2}{1 + \alpha^2} \nabla_{\mathbf{k}} \theta, \quad \mathcal{A}_{s,\mathbf{k}}^\tau = -\frac{1}{2} \mathcal{A}_{0,\mathbf{k}}^\tau. \quad (\text{B3})$$

Consequently, the Berry curvature $\Omega_{n,\mathbf{k}}^\tau = \nabla_{\mathbf{k}} \times \mathcal{A}_{n,\mathbf{k}}^\tau$ is readily obtained as

$$\begin{aligned} \Omega_{s,\mathbf{k}}^\tau &= \frac{\tau}{2} \frac{1 - \alpha^2}{1 + \alpha^2} \nabla_{\mathbf{k}} \times \left(-\frac{k_y}{k_x^2 + k_y^2}, \frac{k_x}{k_x^2 + k_y^2}, 0 \right) \\ &= \tau \frac{1 - \alpha^2}{1 + \alpha^2} \pi \delta(\mathbf{k}) \hat{\mathbf{k}}_z \end{aligned} \quad (\text{B4})$$

for the conical bands and $\Omega_{0,\mathbf{k}}^\tau = -2\Omega_{s,\mathbf{k}}^\tau$ for the flat band, while the Berry phase $\Phi_n^\tau = \oint d\mathbf{k} \cdot \mathcal{A}_{n,\mathbf{k}}^\tau$ for any closed path C_{n,\mathbf{k}_d}^τ encircling a degeneracy point \mathbf{k}_d (i.e., a single valley center) in the momentum space is given by

$$\Phi_s^\tau = \tau \frac{1 - \alpha^2}{1 + \alpha^2} \pi \quad \text{and} \quad \Phi_0^\tau = -2\Phi_s^\tau. \quad (\text{B5})$$

From Eqs. (B4) and (B5), we see that our α - \mathcal{T}_3 system possesses a vanishing Berry curvature except at the band-touching point (or Dirac point) and valley-contrasting Berry phases except for $\alpha = 0$ or 1, which makes the emerging Dirac-type cone an effective singular Berry flux applied perpendicular to the 2D momentum space with a tunable magnitude of $\Phi = (1 - \alpha^2)/(1 + \alpha^2)$. It should be noted that this argument holds for scalar type of perturbation assumed in our work, and since the transport process we investigate occurs away from the Dirac point, the contributing carriers experience vanishing Berry curvatures throughout the process.

APPENDIX C: SCATTERING AMPLITUDE FORMULAS

Minimal model and partial wave expansion. As indicated in the main text, we use the following perturbed Hamiltonian,

$$H = H_0 + V(\mathbf{r}), \quad (\text{C1})$$

to model the quantum scattering processes from the extrinsically controllable impurities such as randomly positioned antidots due to circularly symmetric vertical gates. The impurities are treated as an ensemble of finite-size scattering centers of radius R described by the disordered scalar potential $V(\mathbf{r}) = \sum_i \tau_0 \otimes \mathcal{I}V_0 \Theta(R - |\mathbf{r} - \mathbf{r}_i|)$, which are distributed at random positions \mathbf{r}_i with V_0 being the potential height. The characteristic size R of each individual scatterer is assumed to be much larger than the lattice constant so that intervalley scattering is negligible. If the scatterers are sufficiently dilute so that multiple scattering effects can be ruled out, i.e., the density satisfies $n_{\text{imp}} \ll 1/R^2$, we can impose the single-scattering-event approximation to obtain physically meaningful solutions for the far-field scattering amplitude $f_{\tau\tau'}(\theta)$ using the standard partial wave decomposition (PWD) scheme. In the following, we shall derive its expression in terms of such a single-disk scatterer.

Far away from the scattering center (i.e., $r \gg R$), for an incoming flux along the x direction, the spinor wave function belonging to the valley τ with band index s takes the asymptotic form

$$|\Psi_{s,\tau}^{\gg}(\mathbf{r})\rangle = e^{ikx} |\mathbf{k}_{0,s}\rangle|\tau\rangle + \frac{f_{\tau\tau'}(\theta)}{\sqrt{-ir}} e^{ikr} |\mathbf{k}_{\theta,s}\rangle|\tau'\rangle, \quad (\text{C2})$$

where the Einstein summation convention is applied for the valley index τ' , the ket $|\tau\rangle$ represents the valley state (analogous to the orientation of the isospin along the z axis), and the vector $|\mathbf{k}, s\rangle$ is the spinor plane wave amplitude with wave vectors $\mathbf{k}_0 = (k, 0)$ and $\mathbf{k}_\theta = k(\cos \theta, \sin \theta)$ that define the directions of the incident and scattering waves, respectively. In our system, for the conical dispersion bands $s = \pm$, we have

$$|\mathbf{k}, s\rangle|\tau\rangle = \frac{1}{\sqrt{2}} \begin{pmatrix} \tau \cos \phi e^{-i\tau\theta} \\ s \\ \tau \sin \phi e^{i\tau\theta} \end{pmatrix} |\tau\rangle. \quad (\text{C3})$$

The current operator is defined as $\hat{\mathbf{J}} = (1/\hbar) \nabla_{\mathbf{k}} H(\mathbf{k}) = v_F(\tau_3 \otimes S_x^\phi, \tau_0 \otimes S_y^\phi)$. We thus obtain the scattered current as

$$\begin{aligned} J_{sc} &= \frac{1}{r} \langle \tau' | \langle \mathbf{k}_{\theta,s} | f_{\tau\tau'}^* \hat{\mathbf{J}} \cdot \frac{\mathbf{k}_\theta}{k} f_{\tau\tau'} | \mathbf{k}_{\theta,s} \rangle | \tau' \rangle \\ &= \frac{\tau v_F}{r} [|f_{\tau\tau}(\theta)|^2 + |f_{\tau\bar{\tau}}(\theta)|^2], \end{aligned} \quad (\text{C4})$$

while the incident current is

$$J_{in} = \langle \tau | \langle \mathbf{k}_0, s | \hat{\mathbf{J}} \cdot \mathbf{k}_0 / k | \mathbf{k}_0, s \rangle | \tau \rangle = \tau v_F. \quad (\text{C5})$$

The differential cross section can be calculated from the scattering amplitudes $f_{\tau\tau'}(\theta)$ as

$$\frac{d\Sigma^\tau}{d\theta} = \frac{r J_{sc}}{J_{in}} = |f_{\tau\tau}(\theta)|^2 + |f_{\tau\bar{\tau}}(\theta)|^2, \quad (\text{C6})$$

where $\bar{\tau} \equiv -\tau$, and $f_{\tau\bar{\tau}}(\theta)$ denotes the scattering amplitudes in the valley-flip channels, which vanishes in the absence of intervalley-coupling perturbations. Other relevant cross

sections can be calculated in a similar manner. In particular, the total cross section (TCS) is

$$\Sigma^\tau = \int_0^{2\pi} d\theta \frac{d\Sigma^\tau}{d\theta}, \quad (\text{C7})$$

the transport cross section (TrCS) is

$$\Sigma_{tr}^\tau = \int_0^{2\pi} d\theta (1 - \tau\tau' \cos\theta) |f_{\tau\tau'}(\theta)|^2, \quad (\text{C8})$$

and the skew cross section (SkCS) is given by

$$\Sigma_{sk}^\tau = \int_0^{2\pi} d\theta \tau\tau' \sin\theta |f_{\tau\tau'}(\theta)|^2. \quad (\text{C9})$$

To obtain an exact expression for $f_{\tau\tau'}(\theta)$, we expand the wave functions inside and outside the scatterer as a superposition of partial waves. In particular, for $r > R$ (outside the scatterer) and $r < R$ (inside the scatterer), we have

$$|\Psi_{s,\tau}^>(\mathbf{r})\rangle = \sum_l \psi_{l,s}^>(\mathbf{r})|\tau\rangle \quad (\text{C10a})$$

and

$$|\Psi_{s,\tau}^<(\mathbf{r})\rangle = \sum_l \psi_{l,s}^<(\mathbf{r})|\tau\rangle, \quad (\text{C10b})$$

respectively, where $\psi_{l,s}^>|\tau\rangle$ and $\psi_{l,s}^<|\tau\rangle$ are the partial waves defined in terms of the cylindrical wave eigenfunctions of the reduced Hamiltonian \mathcal{H} , which in the polar coordinates $\mathbf{r} = (r, \theta)$ reads as

$$\mathcal{H} = \hbar v_F \tau \begin{pmatrix} 0 & \cos\phi \hat{L}_\tau & 0 \\ \cos\phi \hat{L}_\tau & 0 & \sin\phi \hat{L}_\tau \\ 0 & \sin\phi \hat{L}_\tau & 0 \end{pmatrix} + \mathcal{V}(r), \quad (\text{C11})$$

with the compact operator

$$\hat{L}_\tau = -i e^{i\tau\theta} \left(\partial_r + i\tau \frac{\partial_\theta}{r} \right),$$

and $\mathcal{V}(r) = \tau_0 \otimes \mathcal{I}V_0 \Theta(R - r)$ being the circularly symmetric scalar type of scattering potential. Since the isotropic perturbation \mathcal{V} is both valley and sublattice independent, it does not break any discrete symmetries and in fact preserves the rotational symmetry of the system. As a result, we have $[\mathcal{H}, \hat{\mathcal{J}}_z] = 0$ with $\hat{\mathcal{J}}_z \equiv -i\hbar\partial_\theta + \tau_3 \otimes \hbar S_z$, analogous to the z component of the total “(pseudo)angular momentum”. In addition, we have $[\tau_3 \otimes \mathcal{I}, \mathcal{H}] = 0$ (i.e., conservation of

valley isospin) due to the absence of intervalley coupling. Consequently, \mathcal{H} acts on the spinor eigenfunctions of $\hat{\mathcal{J}}_z$, which yields

$$\mathcal{H}\varphi_{l,s}|\tau\rangle = E\varphi_{l,s}|\tau\rangle, \quad (\text{C12})$$

where the wave functions $\varphi_l|\tau\rangle$ simultaneously satisfy $\hat{\mathcal{J}}_z\varphi_l|\tau\rangle = \hbar\tau l\varphi_l|\tau\rangle$ with l being an integer. After some algebra, we obtain, for the conical bands (i.e., $s = \pm$),

$$\varphi_{l,s}^{(0,1)}(\mathbf{r})|\tau\rangle = \frac{1}{\sqrt{2\pi}} \begin{pmatrix} \cos\phi h_{l-\tau}^{(0,1)}(qr)e^{-i\tau\theta} \\ ish_{l,s}^{(0,1)}(qr) \\ -\sin\phi h_{l+\tau}^{(0,1)}(qr)e^{i\tau\theta} \end{pmatrix} e^{il\theta}|\tau\rangle, \quad (\text{C13})$$

where $q = |E - \mathcal{V}|/\hbar v_F$ and $s = \text{sign}(E - \mathcal{V})$. The radial function $h_l^{(0)} = J_l$ is the Bessel function and $h_l^{(1)} = H_l^{(1)}$ is the Hankel function of the first kind. The partial waves outside ($r > R$) and inside ($r < R$) the scatterer are given by

$$\psi_{l,s}^>(\mathbf{r})|\tau\rangle = \sqrt{\pi} i^{l-1} [\varphi_{l,s}^{(0)}|\tau\rangle + A_l^{\tau\tau} \varphi_{l,s}^{(1)}|\tau\rangle + A_l^{\tau\bar{\tau}} \varphi_{l,s}^{(1)}|\bar{\tau}\rangle] \quad (\text{C14a})$$

and

$$\psi_{l,s}^<(\mathbf{r})|\tau\rangle = \sqrt{\pi} i^{l-1} [B_l^{\tau\tau} \varphi_{l,s}^{(0)}|\tau\rangle + B_l^{\tau\bar{\tau}} \varphi_{l,s}^{(0)}|\bar{\tau}\rangle], \quad (\text{C14b})$$

respectively, where $A_l^{\tau\tau}$ ($A_l^{\tau\bar{\tau}}$) and $B_l^{\tau\tau}$ ($B_l^{\tau\bar{\tau}}$) denote the elastic (valley-flip) partial wave reflection and transmission coefficients in the angular channel τl , respectively. To obtain explicit expressions of the partial wave coefficients, proper boundary conditions (BCs) are needed.

Boundary conditions. Recalling the commutation relations $[\hat{\mathcal{J}}_z, \mathcal{H}] = 0$ and $[\tau_3 \otimes \mathcal{I}, \mathcal{H}] = 0$, we define a spinor wave function in the polar coordinates as

$$\psi(r, \theta)|\tau\rangle = [\psi_1, \psi_2, \psi_3]^T |\tau\rangle = \begin{pmatrix} \mathcal{R}_1(r)e^{-i\tau\theta} \\ \mathcal{R}_2(r) \\ \mathcal{R}_3(r)e^{i\tau\theta} \end{pmatrix} e^{il\theta}|\tau\rangle, \quad (\text{C15})$$

which satisfies

$$\mathcal{H}\psi|\tau\rangle = E\psi|\tau\rangle. \quad (\text{C16})$$

Substituting Eq. (C15) into Eq. (C16) and eliminating the angular components, we obtain the following one-dimensional, first-order ordinary differential equation for the radial component:

$$-i\tau \begin{pmatrix} 0 & \cos\phi \left[\frac{d}{dr} + \tau \frac{l}{r} \right] & 0 \\ \cos\phi \left[\frac{d}{dr} - \tau \frac{l-\tau}{r} \right] & 0 & \sin\phi \left[\frac{d}{dr} + \tau \frac{l+\tau}{r} \right] \\ 0 & \sin\phi \left[\frac{d}{dr} - \tau \frac{l}{r} \right] & 0 \end{pmatrix} \begin{pmatrix} \mathcal{R}_1(r) \\ \mathcal{R}_2(r) \\ \mathcal{R}_3(r) \end{pmatrix} = \frac{E - V(r)}{\hbar v_F} \begin{pmatrix} \mathcal{R}_1(r) \\ \mathcal{R}_2(r) \\ \mathcal{R}_3(r) \end{pmatrix}. \quad (\text{C17})$$

Directly integrating the radial equation over a small interval $r \in [R - \eta, R + \eta]$ defined about the interface at $r = R$ and then taking the limit $\eta \rightarrow 0$, we obtain

$$\begin{aligned} \mathcal{R}_2(R - \eta) &= \mathcal{R}_2(R + \eta), \\ \cos\phi \mathcal{R}_1(R - \eta) + \sin\phi \mathcal{R}_3(R - \eta) &= \cos\phi \mathcal{R}_1(R + \eta) + \sin\phi \mathcal{R}_3(R + \eta), \end{aligned} \quad (\text{C18a})$$

provided that the potential $V(r)$ and the radial function components $\mathcal{R}_{1,2,3}(r)$ are all finite. Reformulating such continuity conditions in terms of the corresponding wave function yields the desired BCs:

$$\begin{aligned} \psi_2^<(R, \theta) &= \psi_2^>(R, \theta), \\ \cos \phi \psi_1^<(R, \theta) e^{i\tau\theta} + \sin \phi \psi_3^<(R, \theta) e^{-i\tau\theta} &= \cos \phi \psi_1^>(R, \theta) e^{i\tau\theta} + \sin \phi \psi_3^>(R, \theta) e^{-i\tau\theta}. \end{aligned} \quad (\text{C18b})$$

Far-field solutions. Using the asymptotic form of the Hankel function

$$H_l^{(1)}(kr) \sim \sqrt{2/\pi kr} e^{i(kr - l\pi/2 - \pi/4)},$$

and evaluating the outside wave function given in Eq. (C10a) in the far-field region ($r \gg R$), we arrive at

$$\begin{aligned} |\Psi_{s,\tau}^{\gg}(\mathbf{r})\rangle &= e^{ikx} |\mathbf{k}_{0,s}\rangle |\tau\rangle \\ &+ \frac{-i\sqrt{2/\pi k} \sum_l A_l^{\tau\tau'} e^{il\theta}}{\sqrt{-ir}} e^{ikr} |\mathbf{k}_{\theta,s}\rangle |\tau'\rangle. \end{aligned} \quad (\text{C19})$$

From Eqs. (C19) and (C2), we obtain

$$f_{\tau\tau'}(\theta) = -i\sqrt{\frac{2}{\pi k}} \sum_l A_l^{\tau\tau'} e^{il\theta}. \quad (\text{C20})$$

In our system, the valley-flip amplitudes $A_l^{\tau\bar{\tau}}$ and $B_l^{\tau\bar{\tau}}$ vanish due to the absence of intervalley coupling. Consequently, we have $f_{\tau\bar{\tau}} = 0$.

Imposing the BCs [Eq. (C18b)] on the total wave functions of both sides at the interface $r = R$, we have

$$\begin{aligned} B_l^{\tau\tau} J_l(qR) &= ss' [J_l(kR) + A_l^{\tau\tau} H_l^{(1)}(kR)], \\ B_l^{\tau\tau} X_{l,\tau}^{(0)}(qR) &= X_{l,\tau}^{(0)}(kR) + A_l^{\tau\tau} X_{l,\tau}^{(1)}(kR), \end{aligned} \quad (\text{C21})$$

where $X_{l,\tau}^{(0,1)} = h_{l-\tau}^{(0,1)} \cos^2 \phi - h_{l+\tau}^{(0,1)} \sin^2 \phi$. Solving Eq. (C21), we obtain the unknown coefficients as

$$A_l^{\tau\tau} = -\frac{J_l(qR) X_{l,\tau}^{(0)}(kR) - ss' X_{l,\tau}^{(0)}(qR) J_l(kR)}{J_l(qR) X_{l,\tau}^{(1)}(kR) - ss' X_{l,\tau}^{(0)}(qR) H_l^{(1)}(kR)} \quad (\text{C22})$$

and

$$B_l^{\tau\tau} = \frac{H_l^{(1)}(kR) X_{l,\tau}^{(0)}(kR) - X_{l,\tau}^{(1)}(kR) J_l(kR)}{H_l^{(1)}(kR) X_{l,\tau}^{(0)}(qR) - ss' X_{l,\tau}^{(1)}(kR) J_l(qR)}. \quad (\text{C23})$$

Using the basic relations $J_{-l} = (-)^l J_l$ and $H_{-l}^{(1)} = (-)^l H_l^{(1)}$, we obtain the following relations characterizing the intervalley symmetries:

$$A_{-l}^{\tau\tau} = A_l^{\bar{\tau}\bar{\tau}}; \quad B_{-l}^{\tau\tau} = B_l^{\bar{\tau}\bar{\tau}}. \quad (\text{C24})$$

However, there are no such symmetries for the coefficients belonging to the same valley, except for the particular cases of $\alpha = 0$ and 1, where

$$A_{-l}^{\tau\tau} = A_l^{\tau\tau}; \quad B_{-l}^{\tau\tau} = B_l^{\tau\tau} \quad (\text{C25a})$$

for $\alpha = 1$ (dice lattice), and

$$A_{-l}^{\tau\tau} = A_{l+1}^{\tau\tau}; \quad B_{-l}^{\tau\tau} = B_{l+1}^{\tau\tau} \quad (\text{C25b})$$

for $\alpha = 0$ (graphene). The resulting probability density $\rho = \langle \Psi_{s,\tau}(\mathbf{r}) | \Psi_{s,\tau}(\mathbf{r}) \rangle$ and the local current density $\mathbf{j} = \langle \Psi_{s,\tau}(\mathbf{r}) | \hat{\mathbf{J}} | \Psi_{s,\tau}(\mathbf{r}) \rangle$ can be calculated accordingly. Particularly, the exact scattering amplitude $f_{\tau\tau}(\theta)$ can be obtained according to Eq. (C20).

APPENDIX D: DERIVATION OF EQ. (8), ITS VALIDATION, AND RESONANCE FEATURE

It follows from Eqs. (C7)–(C9) and (C20) that the scattering cross sections have their summation forms given by

$$\Sigma^\tau = \frac{4}{k} \sum_{l=-\infty}^{\infty} |A_l^{\tau\tau}|^2, \quad (\text{D1a})$$

$$\Sigma_{lr}^\tau = \Sigma^\tau - \frac{4}{k} \sum_{l=-\infty}^{\infty} \text{Re}[A_l^{\tau\tau} (A_{l+\tau}^{\tau\tau})^*], \quad (\text{D1b})$$

and

$$\Sigma_{sk}^\tau = \frac{4}{k} \sum_{l=-\infty}^{\infty} \text{Im}[A_l^{\tau\tau} (A_{l+\tau}^{\tau\tau})^*]. \quad (\text{D1c})$$

Here, we analyze the low-energy scattering of the 2D massless Dirac-type particles governed by the Hamiltonian given in Eq. (C1). At low energies, i.e., $kR \ll 1$, the scattering is dominated by the lowest channels $l = 0, \pm\tau$. Defining $x \equiv kR$ and $\rho \equiv V_0 R$ and adopting the convention $\hbar v_F = 1$, under the assumption of $x < \rho \ll 1$ (i.e., under-barrier scattering for weak scatterer/barrier), we obtain the coefficients as

$$A_0^{\tau\tau} = -\frac{P_0}{P_0 + iQ_0}, \quad A_\tau^{\tau\tau} = -\frac{P_1}{P_1 + i(4\alpha^2 + Q_1)}, \quad (\text{D2})$$

$$A_{-\tau}^{\tau\tau} = -\frac{P_1 \alpha^2}{P_1 + i(4 + Q_1 \alpha^2)},$$

where $P_0 = \pi x$ and

$$Q_0 = 2 \left(x \ln \frac{\gamma_E x}{2} - \frac{\tau J_0(\rho - x)}{J_\tau(\rho - x)} \right), \quad (\text{D3})$$

with $\ln \gamma_E \approx 0.577 \dots$ being the Euler's constant and P_1, Q_1 given by $[P_1, Q_1] = x[P_0, Q_0]$. Substituting these coefficients into Eq. (D1), we obtain

$$\begin{aligned} \Sigma_{lr}^\tau / R &= \frac{4P_0^2}{x(P_0^2 + Q_0^2)} \left\{ 1 - 4Q_1 \alpha^2 \left[\frac{1}{P_1^2 + (4\alpha^2 + Q_1)} \right. \right. \\ &\quad \left. \left. + \frac{1}{P_1^2 \alpha^4 + (4 + Q_1 \alpha^2)^2} \right] \right\} \end{aligned} \quad (\text{D4})$$

and

$$\begin{aligned} \Sigma_{sk}^\tau / R &= \frac{16P_0^2 P_1 \alpha^2}{x(P_0^2 + Q_0^2)} \left\{ \frac{1}{P_1^2 + (4\alpha^2 + Q_1)} \right. \\ &\quad \left. - \frac{1}{P_1^2 \alpha^4 + (4 + Q_1 \alpha^2)^2} \right\}. \end{aligned} \quad (\text{D5})$$

For the particular cases of $\alpha = 0$ (graphene) and $\alpha = 1$ (dice lattice), we have $\Sigma_{sk}^\tau / R = 0$, indicating absence of valley skew scattering and thus Hall effect associated with it. In the weak

scattering regime ($\rho \ll 1$), the prefactor

$$\frac{P_0^2}{x(P_0^2 + Q_0^2)} \approx \frac{\pi^2 J_1^2(\rho - x)}{4J_0^2(\rho - x)} x \propto x \ll 1$$

is off resonance, while the other factors generally (except for $\alpha = 0, 1$) contain a dual resonance profile in the energy domain. From Eq. (D5), we obtain the resonance condition as

$$Q_1 + 4\alpha^2 = 0 \Rightarrow \frac{x}{\rho} = \frac{\alpha^2}{1 + \alpha^2} \quad (\text{D6a})$$

or

$$Q_1\alpha^2 + 4 = 0 \Rightarrow \frac{x}{\rho} = \frac{1}{1 + \alpha^2}. \quad (\text{D6b})$$

$$\gamma|_{T=0} \equiv \frac{\sum_{sk}^{\tau}}{\sum_{ir}^{\tau}} \approx \frac{4P_1(16 - P_1^2 - Q_1^2)\alpha^2(1 - \alpha^2)(1 + \alpha^2)}{(16^2 + Q_1^4)\alpha^4 + 16Q_1^2(1 + \alpha^8) + 4Q_1\alpha^2(1 + \alpha^4)(16 + Q_1^2)}. \quad (\text{D8})$$

In the limit $\eta \ll 1$, Eq. (D8) can be further simplified as (the subscript $T = 0$ is omitted hereafter for clarity)

$$\begin{aligned} \gamma(\Phi) &\approx \frac{4P_1\alpha^2(1 - \alpha^2)(1 + \alpha^2)}{Q_1^2 + 4Q_1\alpha^2(1 + \alpha^4) + 16\alpha^4} \\ &\simeq \frac{\pi x^2 \frac{\Phi(1-\Phi)}{1+\Phi}}{(1 + \eta)^2[\Phi - (1 - 2\eta)]^2 + 4\eta \frac{\Phi(1-\Phi)}{1+\Phi}}. \end{aligned} \quad (\text{D9})$$

From Eq. (D9), we obtain the asymptotic behaviors in the opposite limits of $\Phi \rightarrow 1$ (massless spin- $\frac{1}{2}$ particles occurring in, e.g., graphene or topological insulators) and $\Phi \rightarrow 0$ (massless spin-1 particles excited in dice lattices and various type synthetic photonic structures) as

$$\gamma(\Phi) \rightarrow \begin{cases} \frac{\pi x^2}{8\eta^2 + 4\eta(1-\Phi)}(1 - \Phi) & \text{for } \Phi \rightarrow 1, \\ \frac{\pi x^2}{(1-\eta)^2 + 4\eta\Phi} \Phi & \text{for } \Phi \rightarrow 0. \end{cases} \quad (\text{D10})$$

To validate these analytical results on resonance and the valley Hall angle quantitatively, we compare them with those from direct numerical calculations. As shown in Fig. 6, there is an excellent agreement between the analytical results for the dual resonance condition given in Eqs. (D6) and (D7) and the corresponding numerical results [cf. Figs. 6(a)–6(d)], and a similar agreement has been obtained for the singular Berry-flux-resolved valley Hall angle in Eq. (D9) [cf. Fig. 6(e)].

For a particular value of the Berry flux, say $\Phi = \frac{1}{2}$ (i.e., $\alpha = 1/\sqrt{3}$) that can be related to the massless Kane fermions observed in recent experiments (see Appendix H below), we can infer from Eq. (D5) that skew scattering will be enhanced due to the emergent dual resonances positioned at/around $\eta = (1 \pm \Phi)/2$, which can be reached by controlling the carrier energy E . Exact calculations show that such enhancements induced by the dual resonant skew scattering are significant and can lead to considerable valley Hall angles with the maximum absolute values $|\gamma|_{\max} \sim 0.8$ for intermediate scatterer strength, e.g., $\rho = 2$, as depicted in Fig. 7(a). From the near-field patterns as illustrated in Figs. 7(b)–7(e) for the valley K (the patterns for the other valley K' are merely mirror images

of those for K with respect to the horizontal axis), we see that remarkable valley-contrasting spatial skew (asymmetric) trappings occur through the formation of unusual fusiform vortices around one side of the boundary. Consequently, the scattering effectively blocks one of the valleys at one side via the skew trapping, generating efficient valley filtering near/at the resonances. This is consistent with the (far-field) valley-contrasting angular distributions of the corresponding DCS as displayed in the insets of Fig. 7(a).

$$\eta_* = \frac{1 - \Phi_*}{2} \quad (\text{D7a})$$

and

$$\eta_{**} = \frac{1 + \Phi_*}{2} \equiv 1 - \eta_*. \quad (\text{D7b})$$

It can be seen that the first resonance occurs at $\eta \in (0, 1/2)$, while the second one lies within $\eta \in [1/2, 1)$.

From Eqs. (D4) and (D5), we obtain the valley skewness (i.e., the valley Hall angle at zero temperature described in the main text) as

APPENDIX E: SYMMETRY CONSIDERATIONS

The concept of symmetry breaking is fundamental and played an important role in the development of modern condensed matter physics. Various physical effects or phenomena can be attributed to the lack of certain discrete symmetries, e.g., the time-reversal symmetry. Insights about our scattering system can be obtained from a symmetry analysis. To be general, we focus on the following perturbed Dirac-type Hamiltonian in two dimensions:

$$\mathcal{H}(\mathbf{k}) = \tilde{\alpha}_x k_x + \tilde{\alpha}_y k_y + \mathcal{V}, \quad (\text{E1})$$

where $(\tilde{\alpha}_x, \tilde{\alpha}_y) = (\tau_3 \otimes S_x^\alpha, \tau_0 \otimes S_y^\alpha)$ and \mathcal{V} denotes the external perturbed potential. The Hamiltonian \mathcal{H} acts on the spinor wave function $\Psi = [\Psi_A^\tau, \Psi_B^\tau, \Psi_C^\tau, \Psi_A^{\bar{\tau}}, \Psi_B^{\bar{\tau}}, \Psi_C^{\bar{\tau}}]^T$ with $\bar{\tau} \equiv -\tau$ and satisfies $\mathcal{H}\Psi = E\Psi$. As done in the work by Beenakker [54], we figure out an explicit representation of the true time-reversal operator given by

$$\mathcal{T} = \tau_1 \otimes \mathcal{I}K|_{\mathbf{k} \rightarrow -\mathbf{k}}, \quad (\text{E2})$$

where \mathcal{I} is the 3×3 identity operator acting on the sublattice space and K denotes the complex-conjugation operator. Note that the true time-reversal operation is of the orthogonal type, which leads to the transformations $\mathcal{T}\Psi = [\Psi_A^{\bar{\tau}*}, \Psi_B^{\bar{\tau}*}, \Psi_C^{\bar{\tau}*}, \Psi_A^{\tau*}, \Psi_B^{\tau*}, \Psi_C^{\tau*}]^T, \mathcal{T}\tilde{\alpha}_{x,y}\mathcal{T}^{-1} = -\tilde{\alpha}_{x,y}$ in the basis adopted and thus interchanges the valleys, consequently reversing the sign of the current $\mathbf{j} = \Psi^\dagger(\tilde{\alpha}_x, \tilde{\alpha}_y)\Psi$. For the Dirac-type Hamiltonian (E1), there is another antiunitary

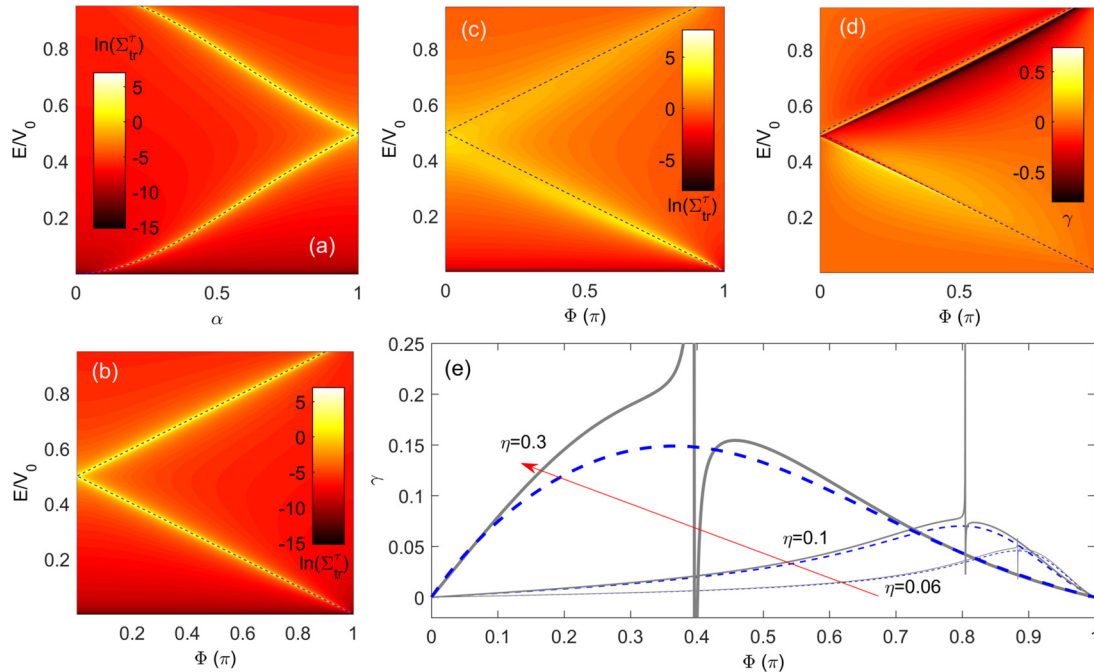


FIG. 6. Validity of analytic results in the low-energy scattering regime. For $x \ll 1$, (a), (b) color-coded natural logarithm of the transport cross section in the coordinates of (α, η) and (Φ, η) , respectively, for scatterer strength $\rho = 0.1$. (c), (d) Color-coded $\ln(\Sigma_{tr}^\tau)$ and zero-temperature valley Hall angle γ as a function of the Berry flux Φ and η for $\rho = 1$. (e) Valley Hall angle γ versus the Berry flux Φ for different values of the reduced carrier energy $\eta = 0.06, 0.1, 0.3$ (along the red arrow). In all panels, the blue curves are calculated from the analytic formulas (D6) and (D7) for the dual resonance condition [cf. (a)–(d)] and Eq. (D9) for the Berry flux dependence of the valley Hall angle [cf. (e)], with the conventions $\{\hbar v_F = 1, x = kR, \rho = V_0R, \eta = E/V_0\}$ (as in the main text).

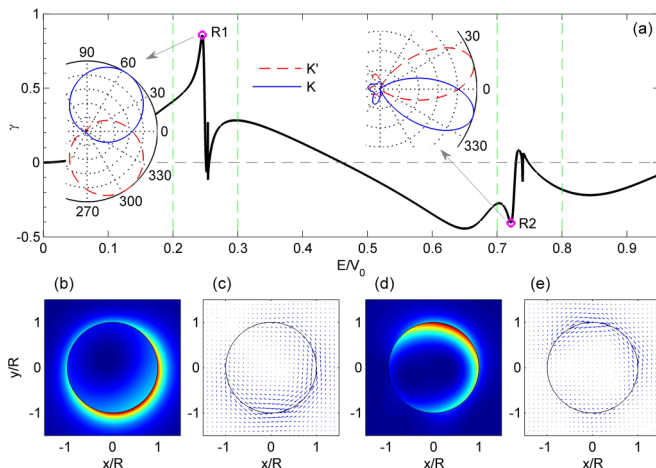


FIG. 7. Enhanced valley Hall angle and valley filtering by resonant skew scattering. (a) Valley Hall angle as a function of carrier energy normalized by the scattering potential height. (b), (c) The near-field patterns of local probability and current density, respectively, associated with the valley K at the resonance indicated by the R1 pink circle in (a). (d), (e) The corresponding near-field patterns associated with another resonance as indicated by the R2 pink circle for the same valley. Insets of (a) are polar plots of the differential cross section for different valleys at two prominent valley Hall angles marked by the pink circles R1 and R2. For all panels, we set $\rho = 2$.

operator defined independently for each valley:

$$\mathcal{T}_e = \begin{cases} \tau_0 \otimes (i\sigma_y \oplus 0) K|_{k \rightarrow -k} & \text{for } \alpha = 0, \\ \tau_0 \otimes \begin{pmatrix} 0 & 0 & -\alpha \\ 0 & 1 & 0 \\ -1/\alpha & 0 & 0 \end{pmatrix} K|_{k \rightarrow -k} & \text{for } \alpha \in (0, 1], \end{cases} \quad (\text{E3})$$

which by definition does not interchange the valleys but reverses the sign of the current associated with each valley. It thus acts as an *effective time-reversal* operator for a single valley.

Distinct from the \mathcal{T} symmetry, the \mathcal{T}_e symmetry can be broken without a magnetic field. Conventionally, this occurs when sublattice/valley-dependent perturbations are present [54]. Remarkably, in our system, we encounter a scenario in which the \mathcal{T}_e symmetry can be broken inherently in the absence of any such sublattice or valley-dependent perturbation, while the \mathcal{T} symmetry is preserved. In particular, for the scalar type of perturbation, i.e., $\mathcal{V} = \tau_0 \otimes \mathcal{I}V_0$ considered in our work, we have $\mathcal{T}\mathcal{V}\mathcal{T}^{-1} = \mathcal{V}$, $\mathcal{T}_e\mathcal{V}\mathcal{T}_e^{-1} = \mathcal{V}$, and thus $\mathcal{T}\mathcal{H}\mathcal{T}^{-1} = \mathcal{H}$ while $\mathcal{T}_e\mathcal{V}\mathcal{T}_e^{-1} \neq \mathcal{H}$ for $0 < \alpha < 1$, indicating that there is no \mathcal{T} symmetry breaking as it should be, but \mathcal{T}_e is in general broken except for the particular cases of $\alpha = 0$ (graphene) and $\alpha = 1$ (dice lattice). The breaking of the \mathcal{T}_e symmetry imposes the following constraints on the scattering coefficients

$$A_l^{\tau\tau} \neq A_{-l}^{\tau\tau}, \quad A_l^{\bar{\tau}\bar{\tau}} \neq A_{-l}^{\bar{\tau}\bar{\tau}}, \quad A_l^{\tau\bar{\tau}} = A_{-l}^{\bar{\tau}\tau}. \quad (\text{E4})$$

Two relations then follow from Eq. (C20): $|f_{\tau\tau}(\theta)| \neq |f_{\tau\tau}(-\theta)|$ and $|f_{\tau\tau}(\theta)| = |f_{\bar{\tau}\bar{\tau}}(-\theta)|$, where the former

accounts for the breaking of the \mathcal{T}_e symmetry and the latter signifies the preservation of the \mathcal{T} symmetry. Consequently, the skew cross section defined in Eq. (C9) is finite and has opposite signs for different valleys, leading to the emergence of a net charge-neutrality valley Hall current. We note that when such an inherent \mathcal{T}_e breaking (i.e., $0 < \alpha < 1$) occurs, the corresponding singular Berry flux is non- π fractional and continuously tunable as a function of α . Therefore, the basic symmetry property analysis provides a consistent and more general physical insight on the singular Berry-flux-mediated exceptional valley skew scattering and hence gVHE uncovered in our work.

APPENDIX F: EXTRINSIC VERSUS INTRINSIC VALLEY HALL EFFECT

Hall effect due to asymmetric transport associated with the spin degree of freedom has been studied extensively, with two types of mechanisms: intrinsic or extrinsic [29,35]. In analogy to the intrinsic spin Hall effect, VHE of the intrinsic type was subsequently proposed through the introduction of a staggered sublattice potential to generate finite valley-contrasting Berry curvatures [2,13]. Extrinsic VHE requires external valley-resolved perturbations such as magnetic fields, strain-induced pseudomagnetic fields, or magnetic materials that have opposite effect on the two valleys [10,11,18–20].

However, our gVHE is distinct and can arise in the absence of nontrivial Berry curvatures and any external valley-dependent perturbation. Unlike the conventional types, the gVHE uncovered here is mediated by inherent singular Berry fluxes in the momentum space with vanishing Berry curvatures and manifests itself through exceptional skew scattering from valley-independent impurities. Our gVHE is thus neither purely intrinsic nor extrinsic but of a hybrid/mixed type of Hall effect.

APPENDIX G: INTERVALLEY SCATTERING

Intervalley scattering can be justifiably neglected in our work, for the following reasons. First, the perturbations in our study are of the scalar type, which is both valley and sublattice independent. That is, the perturbations respect all discrete symmetries of the original Hamiltonian, making the valley degree of freedom (isospin) conserved throughout the scattering process. Second, the valleys separated by a long distance in the momentum space (i.e., $8\pi/3a$ with a being the lattice constant) are robust against perturbations since intervalley scattering occurs only when a large momentum on the order of the inverse lattice spacing for scattering from K' to K' is transferred. Last but not least, the impurity potentials adopted in our work are assumed to be smooth on the lattice scale but sharp in comparison with the carriers' wavelength.

As a matter of fact, in valleytronic applications such as valley current generators (valley “battery”) or a valley carrier of information, a weak intervalley scattering or a long valley relaxation time is needed to generate a robust valley current and preserve coherence. For the honeycomb lattice, it turns out that intervalley scattering is strongly suppressed because of the large separation in the momentum space, offering the possibility of exploiting the valley index in a way

similar to the role of spin in spintronics applications. This makes graphene attractive and competitive for valleytronics applications [2,55]. We note that, in a more recent experiment for the graphene system with sharp, circular scalar-type (electrostatic) potentials as adopted here [56], intervalley scattering is generally not observed and a single valley continuum Dirac Hamiltonian with disk-shaped step potentials is sufficient.

APPENDIX H: MAP ONTO MASSLESS KANE FERMIONS

In recent experiments [51–53], exotic Dirac-type quasiparticles named massless Kane fermions have been observed in 3D zinc-blende crystals, i.e., $\text{Hg}_{1-x}\text{Cd}_x\text{Te}$, at some critical doping concentration. In the presence of strong spin-orbit interaction (e.g., ~ 1 eV), the fermions can be effectively described by the six-band Kane Hamiltonian [51] defined in the basis

$$\{|e \uparrow\rangle, |hh \uparrow\rangle, |lh \uparrow\rangle, |e \downarrow\rangle, |hh \downarrow\rangle, |lh \downarrow\rangle\},$$

that is arranged from the lowest electron conduction band $|e\lambda\rangle$, heavy-hole valance band $|hh\lambda\rangle$ to the light-hole valance band $|lh\lambda\rangle$ separated by the spin index $\lambda = \uparrow, \downarrow$ as

$$H_{\text{Kane}}(\mathbf{k}, k_z) = \begin{pmatrix} 0 & \frac{\sqrt{3}vk_+}{2} & -\frac{vk_-}{2} & 0 & 0 & -vk_z \\ \frac{\sqrt{3}vk_-}{2} & 0 & 0 & 0 & 0 & 0 \\ -\frac{vk_+}{2} & 0 & 0 & -vk_z & 0 & 0 \\ 0 & 0 & -vk_z & 0 & -\frac{\sqrt{3}vk_-}{2} & \frac{vk_+}{2} \\ 0 & 0 & 0 & -\frac{\sqrt{3}vk_+}{2} & 0 & 0 \\ -vk_z & 0 & 0 & \frac{vk_-}{2} & 0 & 0 \end{pmatrix}, \quad (\text{H1})$$

where $k_{\pm} = k_x \pm ik_y$ and $v = \sqrt{3/2}P/m_0$ with P being the Kane's matrix element and m_0 being the free-electron mass. With the unitary transformation

$$\mathcal{S} = \tau_0 \otimes \begin{pmatrix} 0 & 1 & 0 \\ 1 & 0 & 0 \\ 0 & 0 & -1 \end{pmatrix},$$

we obtain

$$\mathcal{H}_{\text{Kane}}(\mathbf{k}, k_z) = \mathcal{S}^\dagger H_{\text{Kane}} \mathcal{S} = v\tilde{\alpha}_x k_x + v\tilde{\alpha}_y k_y + v\tilde{\alpha}_z k_z, \quad (\text{H2})$$

where the matrices $\tilde{\alpha}_{x,y,z}$ (resembling those for Dirac fermions) define the underlying symmetries of the quasiparticles and have the form

$$\begin{aligned} \tilde{\alpha}_x &= \tau_3 \otimes \begin{pmatrix} 0 & \sqrt{3}/2 & 0 \\ \sqrt{3}/2 & 0 & 1/2 \\ 0 & 1/2 & 0 \end{pmatrix}, \\ \tilde{\alpha}_y &= \tau_0 \otimes \begin{pmatrix} 0 & -i\sqrt{3}/2 & 0 \\ i\sqrt{3}/2 & 0 & -i/2 \\ 0 & i/2 & 0 \end{pmatrix}, \\ \tilde{\alpha}_z &= \tau_1 \otimes \begin{pmatrix} 0 & 0 & 0 \\ 0 & 0 & 1 \\ 0 & 1 & 0 \end{pmatrix}. \end{aligned} \quad (\text{H3})$$

From Eq. (H3), we have

$$\tilde{\alpha}_x = \tau_3 \otimes S_x^{\alpha=1/\sqrt{3}} \quad (\text{H4a})$$

and

$$\tilde{\alpha}_y = \tau_0 \otimes S_y^{\alpha=1/\sqrt{3}}. \quad (\text{H4b})$$

Since the subspace on which the Pauli matrices $\tau_{i=1,2,3}$ act hosts real spin instead of the valley isospin, there exists an exact map between the 2D sector of massless Kane fermion system and the generalized lattice model proposed in the main text:

$$\mathcal{H}_{\text{Kane}}(\mathbf{k}, k_z = 0) = H_0(\alpha = 1/\sqrt{3}). \quad (\text{H5})$$

-
- [1] A. Rycerz, J. Tworzydło, and C. W. J. Beenakker, *Nat. Phys.* **3**, 172 (2007).
- [2] D. Xiao, W. Yao, and Q. Niu, *Phys. Rev. Lett.* **99**, 236809 (2007).
- [3] K. Behnia, *Nat. Nanotechnol.* **7**, 488 (2012).
- [4] C. E. Nebel, *Nat. Mater.* **12**, 690 (2013).
- [5] R. V. Gorbachev, J. C. W. Song, G. L. Yu, A. V. Kretinin, F. Withers, Y. Cao, A. Mishchenko, I. V. Grigorieva, K. S. Novoselov, L. S. Levitov, and A. K. Geim, *Science* **346**, 448 (2014).
- [6] X. Xu, W. Yao, D. Xiao, and T. F. Heinz, *Nat. Phys.* **10**, 343 (2014).
- [7] A. Kundu, H. A. Fertig, and B. Seradjeh, *Phys. Rev. Lett.* **116**, 016802 (2016).
- [8] Y. Ye, J. Xiao, H.-L. Wang, Z.-L. Ye, H.-Y. Zhu, M. Zhao, Y. Wang, J.-H. Zhao, X.-B. Yin, and X. Zhang, *Nat. Nanotechnol.* **11**, 598 (2016).
- [9] J. Lu, C. Qiu, M. Ke, and Z. Liu, *Phys. Rev. Lett.* **116**, 093901 (2016).
- [10] V. H. Nguyen, S. Dechamps, P. Dollfus, and J.-C. Charlier, *Phys. Rev. Lett.* **117**, 247702 (2016).
- [11] M. Settnes, S. R. Power, M. Brandbyge, and A.-P. Jauho, *Phys. Rev. Lett.* **117**, 276801 (2016).
- [12] M. Mecklenburg and B. C. Regan, *Phys. Rev. Lett.* **106**, 116803 (2011).
- [13] M. Yamamoto, Y. Shimazaki, I. V. Borzenets, and S. Tarucha, *J. Phys. Soc. Jpn.* **84**, 121006 (2015).
- [14] J. R. Schaibley, H. Yu, G. Clark, P. Rivera, J. S. Ross, K. L. Seyler, W. Yao, and X. Xu, *Nat. Rev. Mater.* **1**, 16055 (2016).
- [15] J. L. Garcia-Pomar, A. Cortijo, and M. Nieto-Vesperinas, *Phys. Rev. Lett.* **100**, 236801 (2008).
- [16] J.-W. Dong, X.-D. Chen, H. Zhu, Y. Wang, and X. Zhang, *Nat. Mater.* **16**, 298 (2017).
- [17] D. Gunlycke and C. T. White, *Phys. Rev. Lett.* **106**, 136806 (2011).
- [18] A. Chaves, L. Covaci, K. Y. Rakhimov, G. A. Farias, and F. M. Peeters, *Phys. Rev. B* **82**, 205430 (2010).
- [19] Y. Jiang, T. Low, K. Chang, M. I. Katsnelson, and F. Guinea, *Phys. Rev. Lett.* **110**, 046601 (2013).
- [20] M. M. Grujić, M. Ž. Tadić, and F. M. Peeters, *Phys. Rev. Lett.* **113**, 046601 (2014).
- [21] M. Trushin and J. Schliemann, *Phys. Rev. Lett.* **107**, 156801 (2011).
- [22] D. Xiao, G.-B. Liu, W. Feng, X. Xu, and W. Yao, *Phys. Rev. Lett.* **108**, 196802 (2012).
- [23] Y. D. Lensky, J. C. W. Song, P. Samutpraphoot, and L. S. Levitov, *Phys. Rev. Lett.* **114**, 256601 (2015).
- [24] J. C. W. Song, P. Samutpraphoot, and L. S. Levitov, *Proc. Natl. Acad. Sci. USA* **112**, 10879 (2015).
- [25] K. F. Mak, K. L. McGill, J. Park, and P. L. McEuen, *Science* **344**, 1489 (2014).
- [26] M. Sui, G. Chen, L. Ma, W.-Y. Shan, D. Tian, K. Watanabe, T. Taniguchi, X. Jin, W. Yao, D. Xiao, and Y. Zhang, *Nat. Phys.* **11**, 1027 (2015).
- [27] Y. Shimazaki, M. Yamamoto, I. V. Borzenets, K. Watanabe, T. Taniguchi, and S. Tarucha, *Nat. Phys.* **11**, 1032 (2015).
- [28] J. Lee, K. F. Mak, and J. Shan, *Nat. Nanotechnol.* **11**, 421 (2016).
- [29] N. Nagaosa, J. Sinova, S. Onoda, A. H. MacDonald, and N. P. Ong, *Rev. Mod. Phys.* **82**, 1539 (2010).
- [30] M. I. Dyakonov and V. I. Perel, *Sov. Phys.-JETP Lett.* **13**, 467 (1971).
- [31] M. I. Dyakonov and V. I. Perel, *Phys. Lett. A* **35**, 459 (1971).
- [32] J. E. Hirsch, *Phys. Rev. Lett.* **83**, 1834 (1999).
- [33] Y. Kato, R. C. Myers, A. C. Gossard, and D. D. Awschalom, *Science* **306**, 1910 (2004).
- [34] J. Wunderlich, B. Kaestner, J. Sinova, and T. Jungwirth, *Phys. Rev. Lett.* **94**, 047204 (2005).
- [35] J. Sinova, S. O. Valenzuela, J. Wunderlich, C. H. Back, and T. Jungwirth, *Rev. Mod. Phys.* **87**, 1213 (2015).
- [36] T. Ando, *J. Phys. Soc. Jpn.* **84**, 114705 (2015).
- [37] G. P. Mikitik and Y. V. Sharlai, *Phys. Rev. Lett.* **82**, 2147 (1999).
- [38] L. Duca, T. Li, M. Reitter, I. Bloch, M. Schleier-Smith, and U. Schneider, *Science* **347**, 288 (2015).
- [39] A. Raoux, M. Morigi, J.-N. Fuchs, F. Piéchon, and G. Montambaux, *Phys. Rev. Lett.* **112**, 026402 (2014).
- [40] J. Ziman, *Principles of the Theory of Solids* (Cambridge University Press, Cambridge, 1972).
- [41] Y. Niimi, M. Morota, D. H. Wei, C. Deranlot, M. Basletic, A. Hamzic, A. Fert, and Y. Otani, *Phys. Rev. Lett.* **106**, 126601 (2011).
- [42] M. Morota, Y. Niimi, K. Ohnishi, D. H. Wei, T. Tanaka, H. Kontani, T. Kimura, and Y. Otani, *Phys. Rev. B* **83**, 174405 (2011).
- [43] L. Liu, C.-F. Pai, Y. Li, H. W. Tseng, D. C. Ralph, and R. A. Buhrman, *Science* **336**, 555 (2012).
- [44] T. Seki, Y. Hasegawa, S. Mitani, S. Takahashi, H. Imamura, S. Maekawa, J. Nitta, and K. Takanashi, *Nat. Mater.* **7**, 125 (2008).
- [45] G.-Y. Guo, S. Maekawa, and N. Nagaosa, *Phys. Rev. Lett.* **102**, 036401 (2009).
- [46] J. Balakrishnan, G. K. W. Koon, A. Avsar, Y. Ho, J. H. Lee, M. Jaiswal, S.-J. Baeck, J.-H. Ahn, A. Ferreira, M. A. Cazalilla, A. H. C. Neto, and B. Ozyilmaz, *Nat. Commun.* **5**, 4748 (2014).
- [47] A. Ferreira, T. G. Rappoport, M. A. Cazalilla, and A. H. C. Neto, *Phys. Rev. Lett.* **112**, 066601 (2014).
- [48] H.-Y. Yang, C. Huang, H. Ochoa, and M. A. Cazalilla, *Phys. Rev. B* **93**, 085418 (2016).

- [49] E. Illes, J. P. Carbotte, and E. J. Nicol, *Phys. Rev. B* **92**, 245410 (2015).
- [50] T. Louvet, P. Delplace, A. A. Fedorenko, and D. Carpentier, *Phys. Rev. B* **92**, 155116 (2015).
- [51] M. Orlita, D. M. Basko, M. S. Zholudev, F. Teppe, W. Knap, V. I. Gavrilenko, N. N. Mikhailov, S. A. Dvoretiskii, P. Neugebauer, C. Faugeras, A.-L. Barra, G. Martinez, and M. Potemski, *Nat. Phys.* **10**, 233 (2014).
- [52] J. D. Malcolm and E. J. Nicol, *Phys. Rev. B* **92**, 035118 (2015).
- [53] F. Teppe, M. Marcinkiewicz, S. S. Krishtopenko, S. Ruffenach, C. Consejo, A. M. Kadykov, W. Desrat, D. But, W. Knap, J. Ludwig, S. Moon, D. Smirnov, M. Orlita, Z. Jiang, S. V. Morozov, V. I. Gavrilenko, N. N. Mikhailov, and S. A. Dvoretiskii, *Nat. Commun.* **7**, 12576 (2016).
- [54] C. W. J. Beenakker, *Rev. Mod. Phys.* **80**, 1337 (2008).
- [55] A. F. Morpurgo and F. Guinea, *Phys. Rev. Lett.* **97**, 196804 (2006).
- [56] C. Gutierrez, L. Brown, C.-J. Kim, J. Park, and A. N. Pasupathy, *Nat. Phys.* **12**, 1069 (2016).